

# Physical interpretation of isothermal remanent magnetization endmembers: New insights into the environmental history of Lake Hovsgul, Mongolia

Karl Fabian<sup>1,2</sup> Valeriy P. Shcherbakov<sup>3,4</sup> Lina Kosareva<sup>4</sup> Danis Nourgaliev<sup>4</sup>

Corresponding author: V. P. Shcherbakov, Geophysical Observatory 'Borok' of Russian Academy of Sciences, Borok, Yaroslavskaya oblast, 152742, Russia. (a.b.shcherb@borok.ru)

<sup>1</sup>Geological Survey of Norway, 7491

Trondheim, Norway

<sup>2</sup>CAGE - Centre for Arctic Gas Hydrate,  
Environment and Climate; Department of  
Geology, University of Tromsø, 9037  
Tromsø, Norway

<sup>3</sup>Geophysical Observatory 'Borok' of  
Russian Academy of Sciences, Borok,  
Yaroslavskaya oblast, 152742, Russia

<sup>4</sup>Institute of Geology and Petroleum  
Technologies, Kazan (Volga region) Federal  
University, Russia

This article has been accepted for publication and undergone full peer review but has not been through the copyediting, typesetting, pagination and proofreading process which may lead to differences between this version and the Version of Record. Please cite this article as  
doi: 10.1002/2016GC006506

© 2016 American Geophysical Union  
Received: Jun 24, 2016; Revised: Oct 27, 2016; Accepted: Oct 28, 2016

**Key Points.**

- New physical interpretation method of isothermal remanent magnetization endmember analysis
- Endmembers in Lake Hovsgul are terrigenous influx, magnetite magnetosomes and biotic/abiotic greigite
- Downcore variation reflects climatic history via anoxic/suboxic sediment conditions

**Abstract.** Acquisition curves of isothermal remanent magnetization for 1057 samples of core KDP-01 from Lake Hovsgul (Mongolia) are decomposed into three endmembers using non-negative matrix factorization. The obtained mixing coefficients also decompose hysteresis loops, back-field, and strong-field thermomagnetic curves into their related endmember components. This proves that the endmembers represent different mineralogical fractions of the Lake Hovsgul sedimentary environment. The method used for unmixing offers a new possibility to apply rock magnetism in paleoecological and paleoclimatic studies. For Lake Hovsgul it indicates that a low-coercivity component with a co-varying paramagnetic phase represents a coarse-grained magnetite fraction from terrigenous influx probably via fluvial transport. A second component with coercivities close to 50 mT is identified as a magnetite fraction related to magnetosomes of magnetotactic bacteria. The third component has coercivities near 85 mT and is identified as greigite of biotic or abiotic origin common in suboxic/anoxic sediments. Significant positive correlations between variations of intensity of all three mineralogical components along the core are found. A rapid drop in all endmember concentrations by

more than one order of magnitude at about 20 m depth testifies to a major change of the environmental or geological conditions of Lake Hovsgul. It possibly is related to the onset of MIS 10 marking the termination of arid climate conditions. Short intervals of high productivity are characterized by an abundance of magnetite magnetosomes and may highlight glacial-interglacial transition intervals. For the rest of the core greigite magnetization substantially exceeds that of magnetite, indicating a predominantly anoxic environment.

Accepted Article

D R A F T

October 26, 2016, 3:13pm

D R A F T

## 1. Introduction

Geological sediments typically contain a complex mixture of magnetic minerals of different origin. Quantitative analysis of the components provides valuable information for reconstructing transport processes, productivity, and environmental conditions at the time of deposition [Evans and Heller, 2003]. Well preserved magnetic minerals in lacustrine sediments can provide paleomagnetic records [Mackereth, 1971; Creer et al., 1972; Thompson, 1973], and contribute to climatic reconstructions [Thouveny et al., 1994]. Integrated effects of physical, chemical, and biological processes ongoing in a lake specify the regime of sedimentation and accordingly the magnetic mineral assemblage within the sediments. Magnetic properties of bottom sediments thus provide proxies for environmental changes and in many cases directly reflect bottom water conditions, for example through abundance and type of bacterial magnetosomes and their conservation [Snowball, 1994; Snowball et al., 2002]. Environmental processes can be traced by variations in concentrations and properties of the magnetic fractions within a sedimentary column.

The possibility to use artificial isothermal magnetization processes to characterize magnetic mineral mixtures was first suggested by Kochegura [1965] who noted the relevance of information contained in the coercivity spectra  $dM_r(B)/dB$  of the isothermal remanent magnetization  $M_r(B)$  where  $B$  is the external field. This approach was developed further by Belokon et al. [1973] and Thompson [1986]. Considerable progress in quantifying the different phases contained in a sample was made by Robertson and France [1994] and Kruiver et al. [2001]. They statistically decomposed the IRM coercivity spectra (CS) into a sum of log-normal distributions whereby each component is fully described by three

parameters: the position of the maximum of the spectrum, spectral width and the magnetization of a given component. *Egli* [2003, 2004a, b] modified this model to account for magnetostatic interactions by replacing the log-normal distributions with generalized log-normal distributions that are described by a larger number of parameters.

The next step towards an unconstrained decomposition was taken by *Heslop and Dillon* [2007] and *Heslop and Roberts* [2012] who applied non-negative matrix factorization (NMF; *Lee and Seung* [2001]) to the decomposition of the coercivity spectra into a prescribed number of endmembers. This method does not require *a priori* knowledge about the distribution functions characterizing specific ferrimagnetic components. Instead, the shapes of the individual components are intrinsically determined by the NMF, which inverts the coercivity spectra of a large collection of samples, assuming that the spectral shape of each sample is a non-negatively weighted sum of these component shapes.

In the present paper we extend the NMF decomposition method of *Heslop and Dillon* [2007] by a tool to attribute the coercivity spectra of the recovered endmembers to mineralogical components. For this we decompose hysteresis loops, backfield curves and high-field thermomagnetic curves by least-square fitting using the weight coefficients of the endmember decomposition. Thereby it is possible to reconstruct hysteresis loops, backfield curves, and high-field thermomagnetic curves of the IRM endmembers which thereby can be interpreted in terms of mineralogical fractions. This interpretation provides new information and insight into paleoclimatic and paleogeographic conditions of Lake Hovsgul during the last million years.

## 2. Setting, Samples, and Methods

### 2.1. Lake Hovsgul core KPD-01

Sediment thickness and paleomagnetic record of the upper  $\approx$ 50 m yield an estimated age of more than 5 Ma for Lake Hovsgul (also transliterated as Khubsugul or Khouvsgol) [Fedotov *et al.*, 2004a; Prokopenko *et al.*, 2009]. This makes it one of the most ancient lakes on Earth.

Its area is 2760 km<sup>2</sup>, whereby its maximal length is 136 km, and its maximal width is 36 km. Due to its large depth of 262 m, Lake Hovsgul is the largest lake of Mongolia by volume, and is considered to be the deepest water reservoir in Central Asia. The water table of the lake is located 1645 m above sea level and its drainage basin is located in North Mongolia (Fig. 1a). The basin is a part of the western margin of the Baikal Rift Zone. Orographically, Lake Hovsgol is surrounded by mountains, a large northern promontory of Mongolia. Although more than 96 streams drain into Lake Hovsgol, its catchment area is relatively small [Dulma, 1979]. The source of the Yihe Horo-Gol river, which provides the largest water influx, is a glacier. In the southern part of the lake (Hatgalsky Bay) lies its only outflow into river Eg (Egiyn Gol), which is the largest tributary of the Selenga river [Dulma, 1979]. The mountainous character causes a predominance of erosion over accumulative processes in the catchment [Rogozin, 1994]. As a consequence, there is a continuous transport of eroded material from the catchment into Lake Hovsgul. At present, Lake Hovsgul is an ultra-oligotrophic, oxygen-rich lake with low primary biological productivity [Dulma, 1979].

The Limnological Institute at the Siberian Branch of the Russian Academy of Sciences (SB RAS) as a part of the Russian-Mongolian joint Khubsugul Drilling Project (KDP)

drilled core KDP-01 in the winter 2002- 2003 using a push-coring device (AR "Irkutskgeologiya") [Prokopenko *et al.*, 2009]. The coring site is located in the center of the lake, at 50°58'24"N, 100°24'33"E in a water depth of 239.3 m. The drill hole reached a maximum depth of 53 m, from which sediment cores with a total length of 48 m were recovered. Coring gaps are due to the applied drilling technology.

In addition, two gravity cores X104 and X106 with lengths of 140 cm (water depth; 238 m) and 130 cm (water depth; 236 m), respectively, were collected at 50°56'07" N, 100°26'56" E and 50°53'01" N, 100°21'22" E. They were sampled in August 2001.

## 2.2. Magnetic measurements

The recovered lake sediments were sampled in 4 cm intervals for paleomagnetic and geochemical studies by KDP members. The magnetostratigraphic record of natural magnetic remanence (NRM) reaches the Brunhes/Matuyama boundary at about 4070 cm and the upper Jaramillo boundary at about 5200 cm [Fedotov *et al.*, 2004b]. Another set of 1057 samples was forwarded from KDP to the paleomagnetic laboratory at the Kazan Federal University for magnetic-mineralogical investigations [Nourgaliev *et al.*, 2005].

Rock magnetic measurements, including IRM acquisition curves up to 0.5 T, were performed on 1057 samples using a coercivity spectrometer at the paleomagnetic laboratory of Kazan Federal University [Iassonov *et al.*, 1998; Nourgaliev *et al.*, 2005]. This instrument synchronously measures remanent and induced magnetization of a sample at room temperature in field steps of less than 0.5 mT up to 500 mT.

Figure 1b-d shows examples of IRM acquisition, backfield and magnetic hysteresis curves as well as six CS of different shape of samples from the collection.

Using a Curie express balance [Burov *et al.*, 1986], the temperature dependence of induced magnetization was measured in air at a heating rate of 100 °C/min up to 700 °C. For estimating the contributions from components with different magnetic hardness, the curves were measured at two intensities of the magnetic field (0.05 T and 0.2 T) and each of these measurements was performed on different subsamples. Two consecutive heating curves are used to detect and quantify mineralogical transformations in a sample. The second curve was measured on the same sample after its cooling to room temperature. Thermomagnetic curves have been measured for 12 out of the 1057 samples. The results are discussed in section 3.2.

A preliminary assessment of the paleoenvironmental information recorded in the magnetic signal of sediments, can be provided by the observation of variations in the intensity of SIRM along the core. Figure 2a shows elevated SIRM intensities at core levels below 20 m. To link this SIRM signal to possible changes in the magnetic mineralogy of the core, the Day plot [Day *et al.*, 1977] for all samples was constructed (Figure 2b). The points of this plot form two clusters (yellow and blue in Fig 2b) that were visually separated by the approximate line:  $M_{rs}/M_s = \frac{0.781}{(H_{cr}/H_c)^{1.338}}$ . A common interpretation of Day plots would assign these two clusters to grain-size mixing lines of magnetic minerals with different magnetic hardness or coercivity, whereby the yellow cluster with higher  $M_{rs}/M_s$  at equal  $H_{cr}/H_c$  represents the magnetically harder phase. By plotting  $M_{rs}/M_s$  against core depth, and color coding the two groups in Figure 2c, a clear separation of their occurrence is revealed. The magnetically harder fraction (yellow) mainly reflects core depths between 20 and 35 m and below 50 m, whilst the magnetically soft fraction (blue) dominates the upper part of the core above 20 m. Also between 35 m and 50 m the soft fraction is more

abundant, but intermittent layers of high coercivity (yellow) are more frequent than in the upper part. To obtain a more objective and physical interpretation of these variations, in the next section the visual clustering is augmented by endmember modeling.

### 2.3. Unmixing and endmember analysis

The NMF endmember modeling approach by *Heslop and Dillon* [2007] assumes that for each of the  $K = 1057$  samples the coercivity spectrum (derivative of IRM curve)  $D_k(k = 1, \dots, K)$  is considered to be a vector  $D_k = (d_{k,f})(f = 1, \dots, F)$  with  $F$  components corresponding to fixed field values. For example, if the field is measured in 1 mT steps up to 200 mT ( $F = 200$ ),  $d_{77,50}$  is the coercivity spectrum of sample  $k = 77$  at,  $f = 50$  mT. Each of the  $N$  endmembers  $E_j = (e_{j,1} \dots, e_{j,F})$  is also a vector with  $F$  components and can be interpreted as the derivative of the corresponding IRM curve. For a physically meaningful endmember it is essential that all components  $e_{j,f}$  are non-negative and that each data set  $D_k$  can be well approximated by a linear combination

$$D_k^* = w_{k,1}E_1 + \dots + w_{k,N}E_N \quad (1)$$

with non-negative coefficients (weights)  $w_{k,1}, \dots, w_{k,N}$ . The requirement of non-negative weights  $w_{k,j} \geq 0$  ensures that the linear combination describes a physical mixture of different physically meaningful components. A negative weight  $w_{k,j}$  would mean that component  $j$  is not present in sample  $k$ , but removed from its mixture, while a negative  $e_{j,f}$  corresponds to a decrease of the IRM curve of endmember  $j$  at field step  $f$  which is also not realistic for natural samples. Non-negative matrix factorization (NMF) techniques, such as that of *Lee and Seung* [2001] exactly strive to achieve such a decomposition in an optimal way by minimizing the Euclidean distance between  $D_k$  and  $D_k^*$ . It should be

noted however that the NMF method does not generate a unique solution and cannot prove that optimal decomposition is reached. Due to the mathematical nature of NMF the final endmembers represent co-varying fractions of the IRM derivatives and *per se* do not represent single minerals or restricted grain-size fractions.

### 3. Results

#### 3.1. Endmember decomposition

From borehole KDP-01 at Lake Hovsgul 1057 smoothed derivatives  $dM_r(B)/dB$  of IRM acquisition curves  $M_r(B)$  determined at fields between 1 mT and 200 mT in steps of 1 mT, covering depths from 106 cm to 5216 cm, have been decomposed into endmembers  $E_j$  using NMF. Smoothing of the measurements was performed by quadratic approximation of each acquisition curve over a sliding window of 10 mT width [von Dobeneck, 1996]. The measurements include values up to 500 mT, but only the interval up to 200 mT contains relevant information because above this value almost all remanent magnetizations are saturated within measurement uncertainty. All components  $e_{j,f}$ ,  $f = 1, \dots, 200$ , of endmember  $E_j$  were normalized, such that

$$M_{rs}(E_j) = \sum_{f=1}^{200} e_{j,f} = 1. \quad (2)$$

This implies that the weight  $w_{k,j}$  physically corresponds to the remanent magnetic moment, which  $E_j$  contributes to the SIRM of sample  $k$ , and accordingly has the unit Am<sup>2</sup>/kg. The prescribed number  $N$  of endmembers was varied between  $N = 1$  and  $N = 5$  leading to increasingly better fits to the data set. If the total misfit for  $N = 1$  is 100%, then the misfits for  $N = 2, 3, 4, 5$  components are 39%, 11%, 5%, 4%. The last two models include fits to outliers and unusual curves as well as to measurement noise.

Improving the total misfit beyond 11% for  $N = 3$  apparently only creates additional components which mainly adapt to noise and outliers. The last significant decrease in misfit was obtained between  $N = 2$  and  $N = 3$ . Therefore,  $N = 3$  is considered to be the inherently optimal choice of  $N$  for this data set.

Figure 3 shows the three normalized endmember spectra for core KDP-01.  $E_1$  represents a low-coercive fraction with a long tail towards higher coercivities,  $E_2$  is a well defined high-coercivity fraction with approximately symmetric distribution around 60 mT.  $E_3$  represents the highest coercivity fraction with peak near 85 mT and extended tail towards higher coercivities of more than 150 mT. This fraction apparently is systematically co-occurring together with a minor low-coercive fraction ranging from 10 mT to 30 mT.

The NMF endmember decomposition provides for each sample  $k$  three non-negative weights  $w_{k,j}, j = 1, 2, 3$  that can be plotted as  $SIRM(E_j, d_k)$  in function of depth  $d_k$  of sample  $k$  (Figure 3, bottom diagram). As is seen from this Figure,  $E_1$  is nearly homogeneously distributed over the core, whilst  $E_2$  and  $E_3$  dominate in the deep part of the core below 20 m, but contribute less in the upper part. Their intensity drops by more than a factor 10 at the transition from 2000 cm to 1950 cm (Figure 3, middle and bottom diagrams). Besides this long-term signal, endmembers  $E_2$  and  $E_3$  vary irregularly on length scales of one to several meters, with numerous distinct outbursts.

The difference in the distribution of the three components over the core is illustrated in Figure 4 which shows the histograms of endmember intensities. The temporally stable contribution of  $E_1$  (Figure 3, top diagram) creates a narrow unimodal distribution of IRM values (Figure 4). The broad histogram of  $E_3$  and especially the almost bimodal

histogram of  $E_2$  reflect more complex distributions from highly variable concentrations during sediment deposition.

### 3.2. Physical interpretation of the endmembers

Interpretation of the found endmembers in geological or physical terms requires additional evidence which links these endmembers to mineralogical components like magnetite, greigite, or different grain-size fractions. Such evidence can be acquired by using the found NMF endmember weights  $w_{k,j}$  to decompose other linear extensive quantities measured on a sufficiently large subset of the original sample set into the same endmembers. The term *linear extensive quantity* here denotes any quantity  $\mu(V)$  measured on a sample of volume  $V$  such that for any real numbers  $\alpha, \beta$ , and volumes  $V_1, V_2$ , the measurement of a mixed sample  $\alpha V_1 + \beta V_2$  results in

$$\mu(\alpha V_1 + \beta V_2) = \alpha \mu(V_1) + \beta \mu(V_2).$$

In rock magnetism, hysteresis loops, backfield curves, and thermomagnetic curves  $M(T)$  in good approximation are linear extensive quantities. Thermomagnetic curves are reliable indicators to identify magnetic minerals based on different Curie temperatures  $T_C$ , or on distinct temperature ranges for chemical alteration during heating. Here a practical method is described to perform the decomposition of linear extensive quantities and thus to predict for example thermomagnetic curves, hysteresis loops, and backfield curves that represent the endmembers themselves.

#### 3.2.1. Thermomagnetic curves

To assign physical meaning to the components found in the previous section – for example as mineralogical components – additional linear extensive quantities measured

on a sufficiently large subset of the original sample set are decomposed according to the mixing coefficients  $w_{k,j}$  from the IRM unmixing using a least square pseudo-inverse.

In the case of thermomagnetic curves data from  $N_c = 12$  samples are available, examples are given in Figure 5b. For each temperature step  $T_i$  the normalized magnetization  $M_{k,i}$  of sample  $k$  at this temperature is approximately the linear mixture of the thermomagnetic magnetizations of the endmembers  $E_1, E_2, E_3$  obtained by IRM unmixing, such that for each temperature  $T_i$  one has  $N_c$  linear equations

$$M_{k,i} = w_{k,1}m_{1,i} + w_{k,2}m_{2,i} + w_{k,3}m_{3,i}, k = 1, \dots, N_c, \quad (3)$$

where  $w_{k,j}$  are the weights from the IRM endmember unmixing. For  $N_c > 3$ , equation (3) describes an overdetermined linear system from which the optimal least-square estimate for the three unit-free numbers  $m_{1,i}, m_{2,i}, m_{3,i}$  can be obtained by multiplication of the data vector  $\mathbf{M}_i = (M_{k,i})_{k=1, \dots, N_c}$  with the pseudo-inverse  $W^+$  of the corresponding weight matrix  $W = (w_{k,j})$ . The thermomagnetic curves that correspond to the endmembers are then determined by  $\mathbf{m}_i = W^+ \mathbf{M}_i$ , where  $\mathbf{m}_i = (m_{j,i})_{j=1, \dots, N}$ . Because  $W^+$  does not depend on  $i$ , this is valid for each temperature  $T_i$  separately. The resulting least-square estimates to the thermomagnetic curves of  $E_1, \dots, E_3$  are shown in Figure 5c. Because the numbers  $m_{j,i}$  are unit-free, they represent the thermal magnetization at temperature  $T_i$  relative to endmember  $E_j$ 's remanent magnetization at room temperature. Note that the above point-wise least square estimate does not enforce any positivity constraints on the magnetization curve. The fact that the reconstructed curves have a physically meaningful shape is therefore not self-evident.

For Lake Hovsgul this procedure yields a physical interpretation of the endmembers, because the thermomagnetic curves in Figure 5c establish a mineralogical differentiation.

Note that for these calculations only the 200 mT curves were used as they cover almost the entire coercive spectra. The blue endmember  $E_1$  in Figure 5c(top), is associated to a monotonously decreasing  $M_s(T)$  curve with a Curie around 570°C which suggests magnetite as the predominant magnetic mineral. The induced magnetization in 200 mT at room temperature is more than  $7 M_{rs}$  which indicates PSD to MD grain sizes. In combination the thermomagnetic data characterize  $E_1$  as a coarse grained magnetite fraction as it typically results from terrigenous influx via fluvial transport, especially in an erosional catchment like Lake Hovsgul. The yellow endmember  $E_2$  in Figure 5c(top) also is clearly associated to a Curie temperature of 570°C but shows a more wavy behaviour below 420°C and an induced magnetization in 200 mT at room temperature of only  $2 M_{rs}$ . Curie temperature and high  $M_{rs}/M_s$  point towards single-domain magnetite, probably of bacterial origin. The wavy shape may be due to the high covariance of  $E_2$  and  $E_3$ , which makes differentiation between these phases more difficult. Finally, the thermomagnetic curve of  $E_3$  in Figure 5c, (top) shows a sharp decrease near 400°C that strongly indicates decomposition of greigite ( $\text{Fe}_3\text{S}_4$ ), which has a decomposition temperature close to 350°C and alters to magnetite near 400°C [Dekkers *et al.*, 2000]. That such a chemical change occurs is confirmed by the magnetite-like second heating curve of  $E_3$  (Figure 5c, bottom). Again, the wavy shape of the first-heating curve and its negative values between 400° C and 500° C probably originate from insufficient differentiation between  $E_2$  and  $E_3$ .

Because the available samples only allowed to measure 12 thermomagnetic curves, the statistical basis for the reconstruction of the endmember curves is weak. In Figure 5a,b the decomposition is therefore tested by directly comparing thermomagnetic curves and endmember decomposition for two extreme examples from the available set. The first

is the specimen at depth 2894 cm which displays a predominantly greigite-like thermomagnetic curve (Figure 5b, top) that agrees perfectly with its endmember decomposition which contain mostly the endmember  $E_3$  (Figure 5a, top). The second example from 1959 cm depth has a clear magnetite like thermomagnetic curve while its IRM spectrum is dominated by endmember  $E_1$  (Figure 5b). Thus for  $E_1$  and  $E_3$  the direct comparison of thermomagnetic curves and IRM spectra for the same specimens confirms the interpretation of the endmembers as specific mineralogical components. Unfortunately, the 12 samples do not contain an equally clear example dominated by  $E_2$ , such that its magnetite like curve can only be reconstructed by the outlined least-square inversion which finally confirms that the IRM endmembers  $E_1, \dots, E_3$  correspond to clearly defined mineralogical components of the magnetic fraction.

### 3.2.2. Hysteresis loop analysis

To gain further information about magnetic mineralogy and grain-size distribution of the endmembers, also the hysteresis loops and backfield curves of all 1057 samples have been inverted using the pseudoinverse  $W^+$  to obtain the least-square approximations of hysteresis loops and backfield curves for the endmembers. Prior to this unmixing, the hysteresis curves have *not* been corrected for their paramagnetic slope at high fields. This slope is physically not connected to the IRM, and contains independent and potentially decisive information. If it varies in correlation with some IRM endmembers, this provides strong evidence that these endmembers indeed represent broader sediment fractions and are relevant for paleoenvironmental interpretations. The loops assigned to the endmembers by unmixing are shown in Figure 6. They provide additional information that is in agreement with the conclusions from the thermomagnetic curves. The hysteresis loop cor-

responding to  $E_1$  resembles a typical multidomain (MD) magnetite hysteresis loop with an additional relatively large paramagnetic slope. This indicates that  $E_1$  represents a mixture of relatively large magnetite grain sizes and paramagnetic phases as they typically occur from fluvial or gravitational transport.

Component  $E_2$  possesses a well defined single-domain (SD) loop. In lacustrine environments this is a fingerprint of magnetosome chains from magnetotactic bacteria, which selectively produce SD magnetite grains in the 30-100 nm range. Surprisingly, the loop clearly is associated with a negative high-field slope which could indicate a substantial amount of co-varying diamagnetic material, for example carbonate. However, the high-field branch of  $E_2$  is not sufficiently straight, and on average has a too high negative slope, such that this simple interpretation appears doubtful. As an alternative it is suggested that the negative slope rather results from a non-linear correlation with  $E_1$ . This could be purely statistical, in that variation of terrigenous influx is related to different sediment surface redox conditions, favoring higher or lower MTB populations. It also could reflect a direct mechanism that removes paramagnetic material and thereby decreases the positive slope, for example if the MTB population preferentially consumes paramagnetic iron phases. This demonstrates the potential of IRM unmixing to recover and trace subtle co-varying processes in sediments.

$E_3$  has an even higher  $H_c$  of 86 mT. By its thermomagnetic behavior  $E_3$  is mineralogically identified as greigite and its hysteresis loop suggests that it mainly represents single-domain particles. This component resembles component BH in Lake Baldegg, where it is characterized as a magnetosome phase resistant to anoxic conditions and suppressed at elevated oxygen concentration [Egli, 2004a, c]. While the latter two properties suggest

an interpretation of  $E_3$  as greigite magnetosomes, the relatively wide dispersion of  $E_3$  (Figure 3) is in conflict with a small dispersion parameter (DP) expected for magnetosome ensembles. Therefore admixture of an uncertain amount of abiotic greigite, common in suboxic/anoxic sediments, has to be assumed to explain the wide range of high IRM coercivities in this component. While in marine environments, the differentiation between bacterial greigite and greigite of abiotic origin is known to be difficult [Rowan *et al.*, 2009; Roberts *et al.*, 2011; Chang *et al.*, 2014], also in lacustrine environments examples for high-coercive abiotic greigite phases have recently been reported by Just *et al.* [2016].

From the reconstructed backfield curves in Figure 6b estimated values of  $H_{cr}$  were obtained, which makes it possible to calculate all standard hysteresis parameters  $M_{rs}/M_s$  and  $H_{cr}/H_c$  for  $E_1, \dots, E_3$ , and add the endmember positions to the Day plot in Figure 2b. The required data are collected in Table 1. Large uncertainties of the Day parameters  $M_{rs}/M_s$  and  $H_{cr}/H_c$ , up to a factor 2 for  $E_2$ , occur because  $M_s$  and  $H_c$  depend on the paramagnetic slope correction for the endmember hysteresis curves. This correction is problematic for inverted endmember loops if they, like  $E_2$ , do not show a clear straight slope at high fields. While  $E_2$  and  $E_3$  essentially delimit the general trends of this diagram at the SD end, the estimated position of  $E_1$  appears to have a somewhat too small  $H_{cr}/H_c$  and too high  $M_{rs}/M_s$ . Both effects seem to be related to the marked potbellied shape of the reconstructed loop for  $E_1$  in Figure 6a which increases  $H_c$  and  $M_{rs}$  and might be due to a partial co-variation of  $E_1$  and a biogenic magnetite fraction that was not incorporated into  $E_2$ .

In short, the interpretation of the hysteresis loops of the endmembers (Figure 6a) can be summarized as follows:

1. The blue endmember loop corresponds to soft magnetic PSD-MD magnetite combined with a paramagnetic fraction. Both mineralogies are characteristic for terrigenous influx into the lake.
2. The yellow endmember has a high coercivity of about 50 mT and a rectangular loop with negative slope which may reflect consumption of Fe ion from paramagnetic environment during the synthesis of magnetosomes.
3. The green endmember loop has the highest coercivity of over 70 mT and shows no slope at high fields. It probably indicates greigite ( $\text{Fe}_3\text{S}_4$ ).

#### 4. Discussion

##### 4.1. Assigning the endmembers to lacustrine sediment components

Based on a detailed analysis of IRM spectra from the alpine Lake Baldegg, Switzerland, *Egli* [2003, 2004a, b] distinguished five ferrimagnetic components common in lake sediments. Three of them coincide in character to the endmembers identified in Lake Hovsgul:

1. The detrital magnetite (D) with maximum coercivity in the interval 0-30 mT agrees very well with component  $E_1$  in Lake Hovsgul and represents fluviatile and gravitational influx. This fluviatile fraction is the least variable fraction over the entire core length corresponding to a period of about 1 Ma.
2. The biogenic soft component (BS) corresponds to  $E_2$  with coercivities the interval of 50-60 mT.  $E_2$  represents authigenic magnetite from magnetotactic bacteria (MTB) which prefer suboxic environments close to the sediment surface.

3. What is indicated as 'biogenic highly coercive fraction (BH)' by *Egli* [2004a] in Lake Baldegg predominantly includes bacterial greigite with coercivities above 70-80 mT and occurs as  $E_3$  in Lake Hovsgul where it may represent abiotic as well as biogenic greigite.

#### 4.2. Analysis of correlations between the endmembers

Figure 3 and Figure 9 show that the intensities of fine grained fractions  $E_2$  and  $E_3$  are positively correlated, marking intervals of enhanced or reduced MTB productivity. Particularly noticeable is the drop in both  $E_2$  and  $E_3$  intensities by an order of magnitude which is seen near the depth of 20 m. This substantial decrease certainly is caused by a major event in the history of Lake Hovsgul. Juxtaposition of rock magnetic data with geochemical data by *Fedotov et al.* [2004b] reveal that the epoch of relatively high MTB activity between 20 and 35 meters corresponds to a high level of salt content which also terminates at the depth of about 20 m. *Fedotov et al.* [2004b] tie the period of high salt concentration to arid climate conditions. Because the only clear time markers for KDP-01 are the Matuyama-Brunhes transition at about 780 ka and the onset of the Jaramillo subchron at 1 Ma, a tentative linear interpolation based on magnetic inclination places the suggested period with arid conditions between 0.7 and 0.42 Myr [*Fedotov et al.*, 2004b]. By the same linear interpolation, the transition from high to low IRM values corresponds to 380 ka close to the onset of marine isotopic stage MIS-10 (374 - 337 ka, *Lisiecki and Raymo* [2005]). According to *Fedotov et al.* [2008], ice volume in the area of Lake Hovsgul reached its maximum in the time interval of the last 450 ka during this stage. The here observed marked drop in IRM intensity could therefore reflect suppression of biogenic activity and termination of terrigenic influx with the onset of complete glacial cover of the lake during MIS-10.

To minimize the influence of noise a quantitative estimation of the correlations between the random variables  $E_1, E_2, E_3$  and  $E_2/E_3$  has been performed using the Kendall rank correlation coefficient  $\tau$  which measures the similarity of the orderings of the data. For  $n$  pairs of observations, two pairs  $(x_i, y_i)$  and  $(x_j, y_j)$ , are concordant if either  $x_i > x_j$  and  $y_i > y_j$ , or if  $x_i < x_j$  and  $y_i < y_j$ . Otherwise the pairs are discordant. The Kendall rank coefficient varies between  $-1 \leq \tau \leq 1$  and is calculated from the number  $n_c$  of concordant pairs and the number  $n_s$  of discordant pairs by

$$\tau = \frac{n_c - n_s}{\frac{1}{2}n(n - 1)}. \quad (4)$$

For  $E_2$  and  $E_3$  one obtains  $\tau = 0.64$ , indicating a very strong positive correlation, although  $E_2$  and  $E_3$  cannot be linearly related but have to be linked in a more complex way. Otherwise the non-negative matrix factorization would have assigned them to a single endmember of co-varying phases. To better resolve details, five-point smoothed versions of  $E_2(x)$ ,  $E_3(x)$  and their ratio are plotted as a function of depth in Figure 9, where Figure 9a,b separately focus on the top 13 m of the core. The figures show that most of time the IRM  $E_3$ , related to greigite, exceeds that of  $E_2$ . However, episodically the ratio  $E_2/E_3$  inverts to a dominance of the magnetite-producing MTB (blue shading in Figure 9a). The ratio  $E_2/E_3$  in Figures 9b,d closely resembles the graphs in Figure 9a,c. This implies that extreme values of  $E_2$  and  $E_3$ , indicating high production of bacterial magnetite and bacterial or abiotic greigite, coincide with predominance of magnetite over greigite IRM. Greigite is likely formed at an early diagenetic phase, shortly after MTB magnetite. Calculation of the corresponding Kendall correlation coefficient of  $\tau = 0.685$  between  $E_2$  and  $E_2/E_3$  confirms this visual pattern.

#### 4.3. Connection to sediment-surface oxygenation

Wherever biogenic magnetite is depleted to  $IRM(E_2) < 20\text{mAm}^2/\text{kg}$ , greigite is still present, and becomes the prevailing biogenic phase (deep orange fillings in Figure 9b). In these intervals the absence of fine grained magnetosomes could be explained by later dissolution. Yet, the general correlation between  $E_2$  and  $E_3$  (Figure 9a,c) contradicts this reasoning because in those intervals, where a sharp drop or step in  $E_2$  may suggest dissolution of fine grained magnetite,  $E_3$  shows exactly the same behavior although greigite is not affected by the same dissolution processes as magnetite. For this reason, and because magnetite-producing bacteria require suboxic conditions, the core sections showing low  $E_2$  and  $E_2/E_3$  values rather indicate more anoxic conditions in the lake sediment due to climatic or environmental variation. In short, suboxic conditions  $E_2/E_3 > 1$  are always linked to high MTB abundance, while anoxic conditions are characteristic for reduced MTB production. This pattern is most pronounced for magnetite-producing bacteria.

#### 4.4. Towards a paleoenvironmental interpretation

Based on this solid magnetic evaluation we now progress to a much more hypothetical interpretation in terms of environmental or climatic change. This requires some note of caution, as best expressed by Egli [2004c]: "... many natural systems, such as lakes, oceans and deserts, are characterized by a strongly non-linear response to gradual climatic changes. ... Multiple stable states are possible, and natural systems can be characterized by the same stable state under different climatic conditions or by different stable states under the same climatic conditions. Therefore, care should be taken in attempting to establish a correlation between magnetic proxies and climate parameters." Having said that, the observed substantial changes from anoxic to suboxic conditions in Lake Hovsgul

will almost certainly result from major environmental changes. They occur on time scales which may very well reflect glacial/interglacial transitions. These timescales appear long enough to interpret magnetic signals not solely in terms of non-linear response to a gradual change, but as really reflecting substantial change in the sedimentary environment. For example, melting of glaciers in the catchment will lead to increased influx of organic and inorganic matter and increase productivity, including that of magnetotactic bacteria.

Rapid growth of the MTB population during glacial-interglacial transitions agrees with increased total organic carbon and sulfur concentrations reported for two adjacent, but shorter, sediment cores, X104 and X106, covering the last glacial to postglacial (LG-PG) transition [Nara *et al.*, 2010]. According to their interpretation, dissolved sulfate during the LG accumulated on the shore in wetlands and marshes. Afterwards, increases of precipitation and glacial meltwater influx, and lake level increases during the LG-PG transition could have contributed to the large supply of the  $\delta^{34}S$ -rich dissolved sulfate to deeper parts of Lake Hovsgol [Nara *et al.*, 2010]. The authors conclude that their results indicate an increase of dissolved sulfate concentrations in lake waters and high activity of sulfate reducing bacteria in the sediments during the last glacial to postglacial transition, between 21 kyr to 11.6 kyr BP.

Despite the difficulties to establish a correlation between magnetic proxies and climate parameters, there exists a slight but statistically significant relation between high activity of MTB during glacial to postglacial transitions and increase of sulfate mineral concentration dissolved in distilled water (data provided by Fedotov *et al.* [2008]). By plotting  $E_2 + E_3$  as a proxy for biogenic productivity, and sulfate concentration  $\text{SO}_4$  against depth (Figure 7), a drop in intensity at depths around 20 meters is clearly reflected in both

curves. Besides this common feature, also other peaks coincide between the curves (Figure 7). The three most prominent peaks in Figure 7 lie close to the estimated end of the cold marine isotope stages MIS-4, MIS-5b and MIS-5d, marked by bars in Figure 8b. The Kendall rank coefficient between  $E_2 + E_3$  and SO<sub>4</sub> is  $\tau = 0.15$ , reflecting only a weak correlation, but with a p-value < 0.01. Thus the null hypothesis of statistical independence of  $E_2 + E_3$  and sulfate concentration is rejected on a significance level below 1%, which supports the idea of a link between the increase of dissolved sulfate concentrations in lake waters and high activity of MTB in the sediments during glacial-postglacial transitions.

It is a plausible scenario that  $E_2$ ,  $E_3$  and  $E_2/E_3$  increase in response to increased influx of glacial meltwater, supplying dissolved ions and terrigenous material from the catchment, mainly at glacial-interglacial transitions. Assuming that this connection can be extrapolated back in time, the magnetic data from KDP-01 can be used to detect and quantify similar transitions in previous periods. A number of corresponding short intervals of increased intensities of  $E_2$  and  $E_3$  are clearly recognized in Figure 9a. It is tempting to tie them to the first odd marine oxygen-isotope stages, but unfortunately the available age-depth information for KDP-01 does not provide sufficient resolution to verify this claim.

Oligotrophic lakes like today's Lake Hovsgul are low in organics but rich in oxygen. However, during glacial conditions reduced mixing and reduced influx of terrigenous material and nutrients leads to depletion of oxygen in the sediment surface layer. Together with increased lake-water salinity during cold periods due to lake-level lowstands [Phedorin et al., 2008], this may preferentially stimulate greigite production over bacterial magnetite production. Whilst sulfate experiences only slight reduction in the upper oxidizing zone,

organic matter is reduced such that sulfur becomes abundant a few cm below in the reduction zone forcing the MTB fauna to move deeper while favoring greigite production. Corresponding intervals of extremely low  $E_2$  intensity and low  $E_2/E_3$  ratio are present in Figure 9. By the same argument as above, these local minima between the peaks of  $E_2$  intensity and  $E_2/E_3$  ratio may be related to the even marine oxygen stages. To adapt to changes in the suboxic/anoxic conditions in the course of glacial-interglacial transitions, the MTB population may partially have changed from magnetite to greigite producing biominerization [Bazylinski *et al.*, 1995; Kopp and Kirschvink, 2008]. A recent finding by Lefévre *et al.* [2011] even demonstrates that an individual "greigite-producing magnetotactic bacterium . . . is able to biomineralize greigite and magnetite depending on culture conditions." This flexibility could explain significant variations in the ratio between the content of different types of magnetosomes simply as the response of single MTB species to change of the prevailing environmental condition, whereby the production of greigite depends also on the availability of sulfate in the lake water.

An outstanding feature of the KDP-01 magnetic record is the sharp step at a depth of about 20 m in Figure 9. Here the intensities of both  $E_2$  and  $E_3$  decrease by almost a factor of 100, while the intensity of  $E_1$  drops by a factor of at most 2-3 (Figure 3 and Figure 10). Assuming temporally constant terrigenous influx, the *decrease* of  $E_1$  would indicate an *increase* of sedimentation rate by a factor of 2-3 at the 20 m discontinuity. The additionally deposited material then would be due to authigenic production in the lake, for example from increased plankton deposition. Such a change would rather transport more nutrients into the sediment and does not explain the concomitant drop of  $E_2$  and  $E_3$ . Alternatively, a reduction of terrigenous magnetite supply due to a change in transport processes or

catchment structure may be related to conditions with coincidental low production of  $E_2$  and  $E_3$  in the surface sediment. The variation in concentration of terrigenous magnetite  $E_1$  is indeed also reflected in the intensity of  $E_2$  and the ratio  $E_2/E_1$  (Figure 10), although the correlation is much weaker ( $\tau = 0.20$ ) than in case of the endmembers  $E_2$ ,  $E_3$  and their ratio  $E_2/E_3$  (Figure 9). This observation points to an existence of links between the degree of MTB activity and ongoing processes in the catchment of the lake. Most likely, these links are indirect consequences of climatic changes in the environment of the lake.

## 5. Conclusions

Endmember decomposition of the spectra of 1057 IRM acquisition curves from core KDP-01 results in three main magnetic components which by linear inversion can be assigned to clearly separate hysteresis loops and thermomagnetic curves. This allows to identify these endmember components as three mineralogical components that define the magnetic sediment fraction of Lake Hovsgul over more than 1 Myr. The first component is magnetite with low coercivity and covariant with the paramagnetic sediment phase, indicating a larger magnetic grain-size fraction from terrigenous, probably fluvial influx. The other two components are single-domain fractions with different magnetic hardness, thermomagnetically identified as magnetite and greigite. Their inferred hysteresis loops have no paramagnetic slope, and resemble characteristics of magnetosomes from magnetotactic bacteria, although for the greigite phase abiotic formation is equally possible. The variations of all three magnetic fractions are correlated, whereby strongest correlation occurs between the two single-domain endmembers. The intrinsic linearity of the endmember decomposition implies that these correlations are *not* linear, so during the intervals of high total productivity of magnetotactic bacteria the intensity of magnetite

exceeds that of greigite, while otherwise the ratio between magnetite and greigite signals is considerably less than 1. It appears likely that a high magnetite/greigite ratio indicates suboxic sediment conditions, whilst low values indicate anoxic conditions. The observed periodic variation of this ratio is therefore likely a sensitive climatic proxy marking glacial-interglacial transition intervals versus glacial periods. The here developed new method for linking IRM endmembers to magneto-mineralogical sediment phases thus provides important information about the climatically influenced surface sediment conditions in relation to terrigenous influx, thus connecting two essential processes for the reconstruction of the total lacustrine environment.

**Acknowledgments.** The authors are very grateful to A. P. Fedotov who kindly provided us with the sulfate and salt data for KDP-01. We are very thankful to Simo Spassov and an anonymous reviewer for their valuable comments. The work was carried out according to the Russian Governments Program of Competitive Growth of Kazan Federal University and the grant from Ministry of Science and Education of Russian Federation Contract 14.Z50.31.0017. KF acknowledges funding through NGU and the Centre of Excellence: Arctic Gas hydrate, Environment and Climate (CAGE) funded by the Norwegian Research Council (grant No. 223259). Any additional data may be obtained from Lina Kosareva (email: lina.kosareva@mail.ru).

## References

- Bazylinski, D., R. Frankel, B. Heywood, S. Mann, J. King, P. Donaghay, and A. Hansson (1995), Controlled biomineralization of magnetite ( $\text{Fe}_3\text{O}_4$ ) and greigite ( $\text{Fe}_3\text{S}_4$ ) in a magnetotactic bacterium, *Appl. Environ. Microbiol.*, 61, 3232–3239.

- Belokon, V., V. Kochegura, and L. Sholpo (1973), *Metody paleomagnitnykh issledovanii gornykh porod (Methods of Paleomagnetic Studies of Rocks)*, Nedra, Leningrad.
- Burov, B., D. Nurgaliev, and P. Yasonov (1986), *Paleomagnetic analysis (in Russian)*, KGU, Kazan.
- Chang, I., L. and Vasiliev, C. van Baak, W. Krijgsman, M. J. Dekkers, A. P. Roberts, J. D. Fitz Gerald, A. van Hoesel, and M. Winklhofer (2014), Identification and environmental interpretation of diagenetic and biogenic greigite in sediments: A lesson from the Messinian Black Sea, *Geochem. Geophys. Geosyst.*, 15, 3612–3627, 10.1002/2014GC005411.
- Creer, K., R. Thompson, L. Molyneux, and F. Mackereth (1972), Geomagnetic secular variation recorded in the stable magnetic remanence of recent sediments, *Earth and Planetary Science Letters*, 14, 115–127.
- Day, R., M. Fuller, and V. Schmidt (1977), Hysteresis properties of titanomagnetites: grain-size and compositional dependence, *Phys. Earth Planet. Inter.*, 13, 260–267.
- Dekkers, M. J., H. F. Passier, and M. A. A. Schoonen (2000), Magnetic properties of hydrothermally synthesised greigite ( $\text{Fe}_3\text{S}_4$ ) – II. High- and low- temperature characteristics, *Geophys. J. Int.*, 141, 809–819.
- Dulma, A. (1979), Hydrobiological outline of the Mongolian lakes, *Int. Revue ges. Hydrobiol.*, 64, 709–736.
- Egli, R. (2003), Analysis of the field dependence of remanent magnetization curves, *Journal of Geophysical Research-Solid Earth*, 108(B2).
- Egli, R. (2004a), Characterization of individual rock magnetic components by analysis of remanence curves, 1. unmixing natural sediments, *Studia Geophysica Et Geodaetica*,

- 48(2), 391–446.
- Egli, R. (2004b), Characterization of individual rock magnetic components by analysis of remanence curves. 2. fundamental properties of coercivity distributions, *Physics and Chemistry of the Earth*, 29(13-14), 851–867.
- Egli, R. (2004c), Characterization of individual rock magnetic components by analysis of remanence curves. 3. bacterial magnetite and natural processes in lakes, *Physics and Chemistry of the Earth*, 29(13-14), 869–884.
- Evans, M. E., and F. Heller (2003), *Environmental Magnetism*, Academic Press, Amsterdam.
- Fedotov, A., E. Chebykina, M. Semenov, S. Vorobyova, and *et al.* (2004a), Changes in the volume and salinity of Lake Khubsugul, (Mongolia) in response to global climate changes in the Upper Pleistocene and the Holocene, *Palaeogeogr., Palaeoclimatol., Palaeoecol.*, 209, 245257.
- Fedotov, A., A. Kazansky, D. Tomurhuu, G. Matasova, G. Ziborova, T. Zheleznyakova, S. Vorobyova, M. Phedorin, E. . Goldberg, T. Oyunchimeg, T. Narantsetseg, E. Vologina, A. Yuldashev, I. Kalugin, O. Tomurtogoo, and M. Grachev (2004b), A 1-Myr record of paleoclimates from Lake Khubsugul, Mongolia, *EOS*, 85(40), 387–390.
- Fedotov, A., M. Phedorin, M. De Batist, G. Ziborova, A. Yu Kazansky, M. Yu Semenov, G. Matasova, A. Khabuev, S. Kugakolov, S. Rodyakin, S. Krapivina, and T. Pouls (2008), A 450-ka long record of glaciation in Northern Mongolia based on studies at Lake Khubsugul: high- resolution reflection seismic data and grain-size variations in cored sediments, *Journal of Paleolimnology*, 39, 335–348.

- Heslop, D., and M. Dillon (2007), Unmixing magnetic remanence curves without a priori knowledge, *Geophysical Journal International*, 170(2), 556–566.
- Heslop, D., and A. P. Roberts (2012), A method for unmixing magnetic hysteresis loops, *Journal of Geophysical Research-Solid Earth*, 117.
- Iassonov, P., D. Nourgaliev, B. Bourov, and F. A. Heller (1998), A modernized coercivity spectrometer, *Geologica Carpathica*, 49, 224–226.
- Just, J., N. Nowaczyk, L. Sagnotti, A. Francke, H. Vogel, J. Lacey, and B. Wagner (2016), Environmental control on the occurrence of high-coercivity magnetic minerals and formation of iron sulfides in a 640ka sediment sequence from lake ohrid (balkans), *Biogeosciences*, 13, 2093–2109.
- Kochegura, V. (1965), On the analysis of the curve of normal remanent magnetization, in *Nastoyashchee i proshloe mag nitnogo polya Zemli (The Present and the Past of the Earth's Magnetic Field)*, pp. 154–157.
- Kopp, R., and J. L. Kirschvink (2008), The identification and biogeochemical interpretation of fossil magnetotactic bacteria, *Earth-Science Reviews*, 86, 42–61.
- Kruiver, P. P., M. J. Dekkers, and D. Heslop (2001), Quantification of magnetic coercivity components by the analysis of acquisition curves of isothermal remanent magnetisation, *Earth and Planetary Science Letters*, 189(3-4), 269–276.
- Lee, D., and H. Seung (2001), Algorithms for non-negative matrix factorization, in *Advances in Neural Information Processing Systems 13: Proceedings of the 2000 Conference*, p. 556 562, MIT Press.
- Lefévre, C. T., N. Menguy, F. Abreu, U. Lins, M. Psfai, T. Prozorov, D. Pignol, R. B. Frankel, and D. A. Bazylinski (2011), A cultured greigite-producing magnetotactic bac-

- terium in a novel group of sulfate-reducing bacteria, *Science*, 334, 1720–1723.
- Lisiecki, L. E., and M. E. Raymo (2005), A Pliocene-Pleistocene stack of 57 globally distributed benthic  $\delta^{18}\text{O}$  records, *Paleoceanography*, 20, PA1003, doi:10.1029/2004PA001,071.
- Mackereth, F. (1971), On the variation of the direction of the horizontal component of the remanent magnetization in lake sediments, *Earth and Planetary Science Letters*, 12, 332–338.
- Nara, F. W., T. Watanabe, T. Kakegawa, H. Seyama, K. Horiuchi, T. Nakamura, A. Imai, N. Kawasaki, and T. Kawai (2010), Climate control of sulfate influx to Lake Hovsgol, northwest Mongolia, during the last glacialpostglacial transition: Constraints from sulfur geochemistry, *Palaeogeography Palaeoclimatology Palaeoecology*, 298, 278–285.
- Nourgaliev, D., P. Yasonov, L. Kosareva, A. Kazanskii, and A. Fedotov (2005), The origin of magnetic minerals in the Lake Khubsugul sediments (Mongolia), *Rus. J. Earth Sci.*, 7, 1–6.
- Phedorin, M. A., A. P. Fedotov, S. S. Vorobieva, and G. A. Ziborova (2008), Signature of long supercycles in the Pleistocene history of Asian limnic systems, *J. Paleolimnol.*, 40, 445–452.
- Prokopenko, A. A., M. I. Kuzmin, H. C. Li, K. S. Woo, and N. R. Catto (2009), Lake Hovsgol basin as a new study site for long continental paleoclimate records in continental interior asia: General context and current status introduction, *Quaternary International*, 205, 1–11.
- Roberts, A., L. Chang, C. Rowan, C. Horng, and F. Florindo (2011), Magnetic properties of sedimentary greigite ( $\text{Fe}_3\text{S}_4$ ): An update, *Rev. Geophys.*, 49, 1–46, RG1002.

- Robertson, D. J., and D. E. France (1994), Discrimination of remanence-carrying minerals in mixtures, using isothermal remanent magnetization acquisition curves, *Physics of the Earth and Planetary Interiors*, 82(3-4), 223–234.
- Rogozin, A. (1994), *Limnology and paleolimnology of Mongolia (in Russian)*, 304 pp., Nauka, St. Petersburg.
- Rowan, C., A. Roberts, and T. Broadbent (2009), Reductive diagenesis, magnetite dissolution, greigite growth and paleomagnetic smoothing in marine sediments: A new view, *Earth Planet. Sci. Lett.*, 277, 223– 235.
- Snowball, I., L. Zillen, and P. Sandgren (2002), Bacterial magnetite in swedish varved lake-sediments: a potential bio-marker of environmental change, *Quaternary International*, 88, 13–19, times Cited: 47 4th European Lake Drilling Programme Workshop (ELDP) Sep, 1999 Univ lund, lund, sweden.
- Snowball, I. F. (1994), Bacterial magnetite and the magnetic-properties of sediments in a swedish lake, *Earth and Planetary Science Letters*, 126(1-3), 129–142.
- Thompson, R. (1973), Paleolimnology and paleomagnetism, *Nature*, 242, 182–184.
- Thompson, R. (1986), Modelling magnetization data using simplex, *Phys. Earth Planet. Inter.*, 42, 113–127.
- Thouveny, N., J. L. Debeaulieu, E. Bonifay, K. M. Creer, J. Guiot, M. Icole, S. Johnsen, J. Jouzel, M. Reille, T. Williams, and D. Williamson (1994), Climate variations in europe over the past 140-kyr deduced from rock magnetism, *Nature*, 371(6497), 503–506, times Cited: 237.
- von Dobeneck, T. (1996), A systematic analysis of natural magnetic mineral assemblages based on modelling hysteresis loops with coercivity-related hyperbolic basis functions,

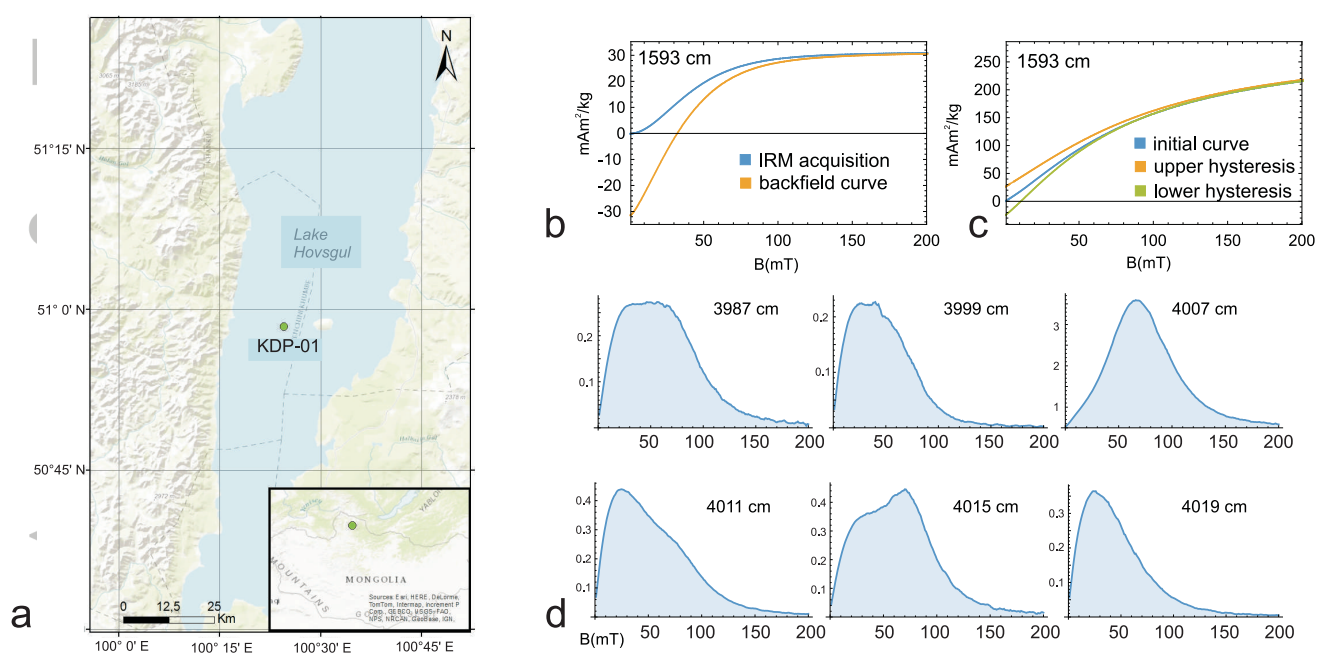


**Figure 1.** a) Geographic location of Lake Hovsgul and position of core KPD-01. b) Example of IRM acquisition and backfield curves up to 200 mT at 1593 cm in KPD-01; c) Corresponding hysteresis curves up to 200 mT at 1593 cm in KPD-01; d) Six examples of IRM coercivity spectra for samples from a narrow depth interval around 4000 cm. The spectrum of a measured IRM acquisition curve at field  $B$  was obtained by robustly fitting a parabola to the measurement data in the interval  $(B - 5\text{mT}, B + 5\text{mT})$  and calculating its derivative at  $B$ . The coercivity spectrum thus corresponds to a smoothed derivative of the IRM acquisition curve between 0 and 200 mT in steps of 1 mT.

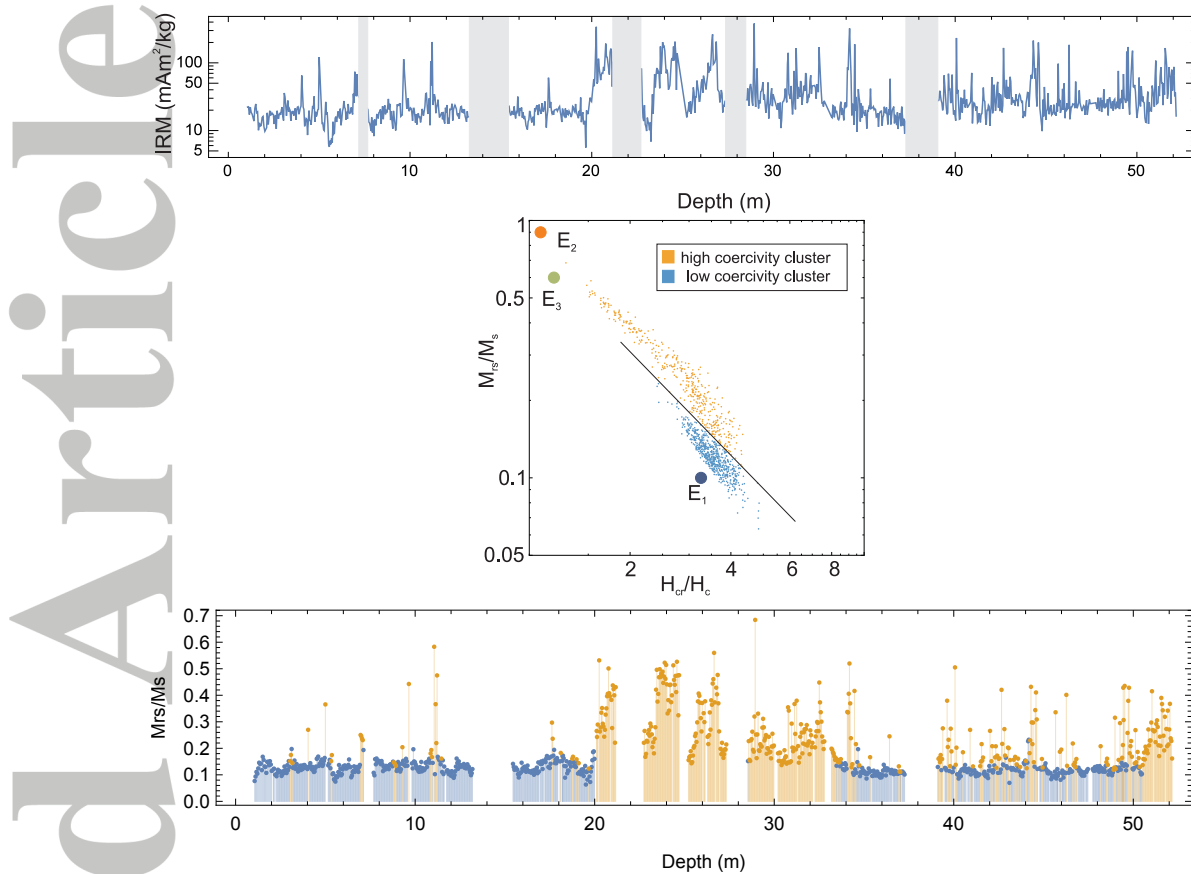


**Figure 2.** a: Logarithmic plot of  $M_{rs}$  = SIRM (at 500 mT) for Lake Hovsgul core KPD-01. Light gray depth intervals indicate sampling gaps. b: Day plot of hysteresis data for Lake Hovsgul core KPD-01. Points  $E_1-E_3$  are explained in the results section. c: Plot of  $M_{rs}/M_s$  for Lake Hovsgul core KPD-01. Extremely high values above 0.5 are likely due to insufficient saturation of the induced magnetization in the maximally applied field of 500 mT. This indicates the presence of magnetic minerals with higher coercivity than that of magnetite. The two groups from the Day plot outline depth intervals with different magnetic mineralogy.

**Table 1.** Estimated endmember hysteresis parameters. Estimates of  $M_{rs}/M_s$  and  $H_c$  have large uncertainties

related to the inverse modeling of the hysteresis loop.

	$E_1$	$E_2$	$E_3$
$M_{rs}/M_s$	0.1	$\approx 0.9$	$\approx 0.6$
$H_{cr}$ (mT)	26	53	86
$H_c$ (mT)	8	49	73
$H_{cr}/H_c$	3.25	1.08	1.18

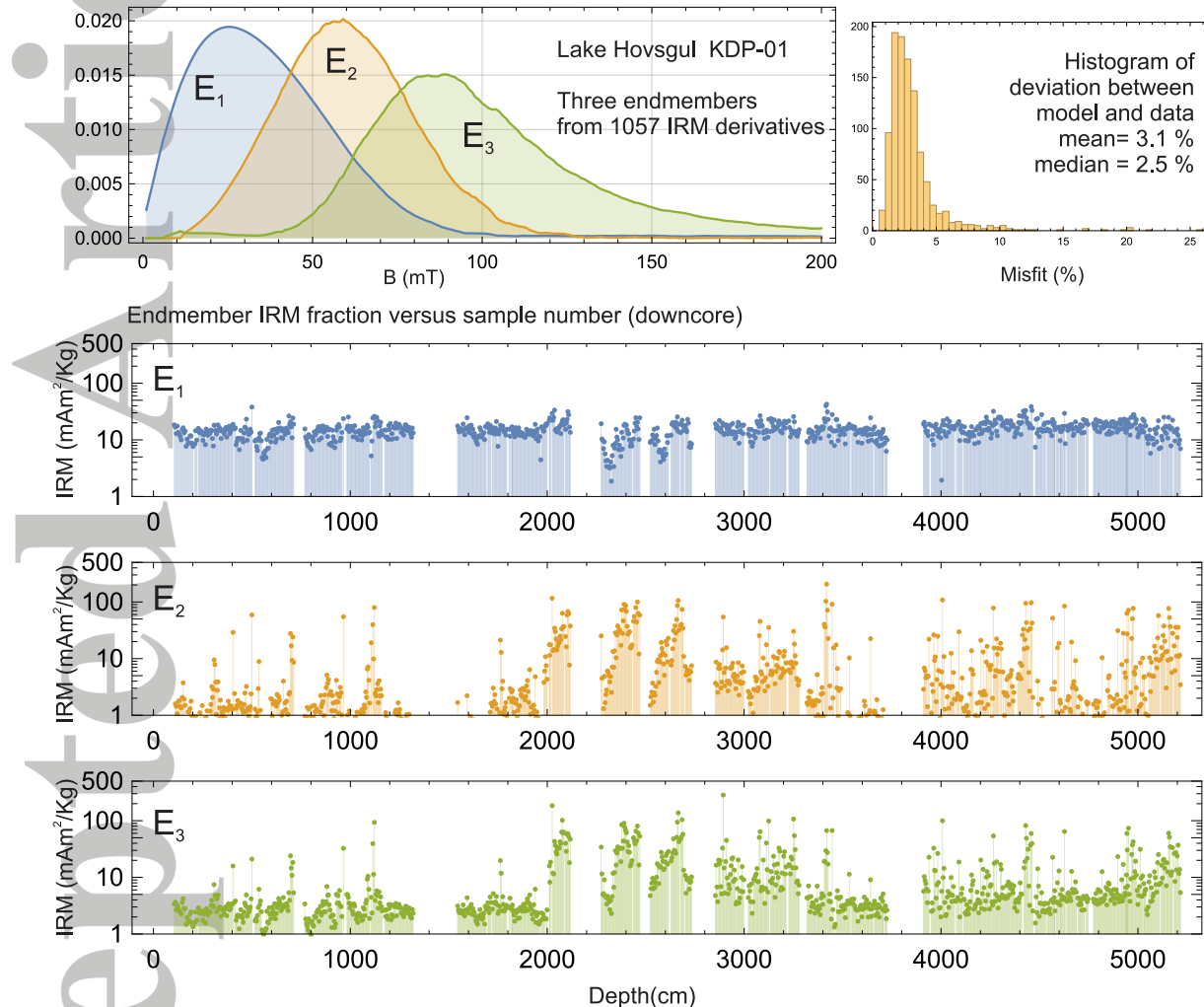


**Figure 3.** Top left: Endmembers  $E_1$ ,  $E_2$ , and  $E_3$  for IRM spectra of Lake Hovsgul sediments. Top right: Histogram of deviation between the endmember model based on  $E_1$ ,  $E_2$ ,  $E_3$  and data. Bottom: Endmember composition versus sample number

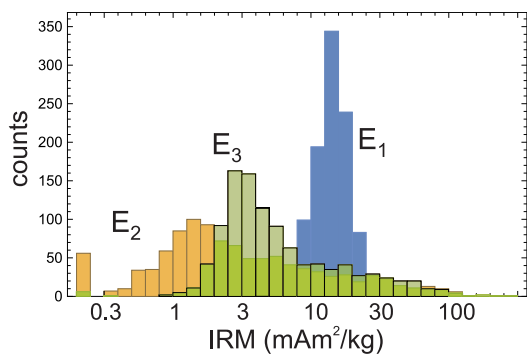


**Figure 4.** Histograms of endmember IRM intensity distributions on a logarithmic scale.  $E_1$  has a narrow unimodal distribution of IRM values.  $E_2$  and  $E_3$  have more complex distribution patterns. They are either almost absent in some parts of the core, but contribute the dominant IRM fractions in other parts.

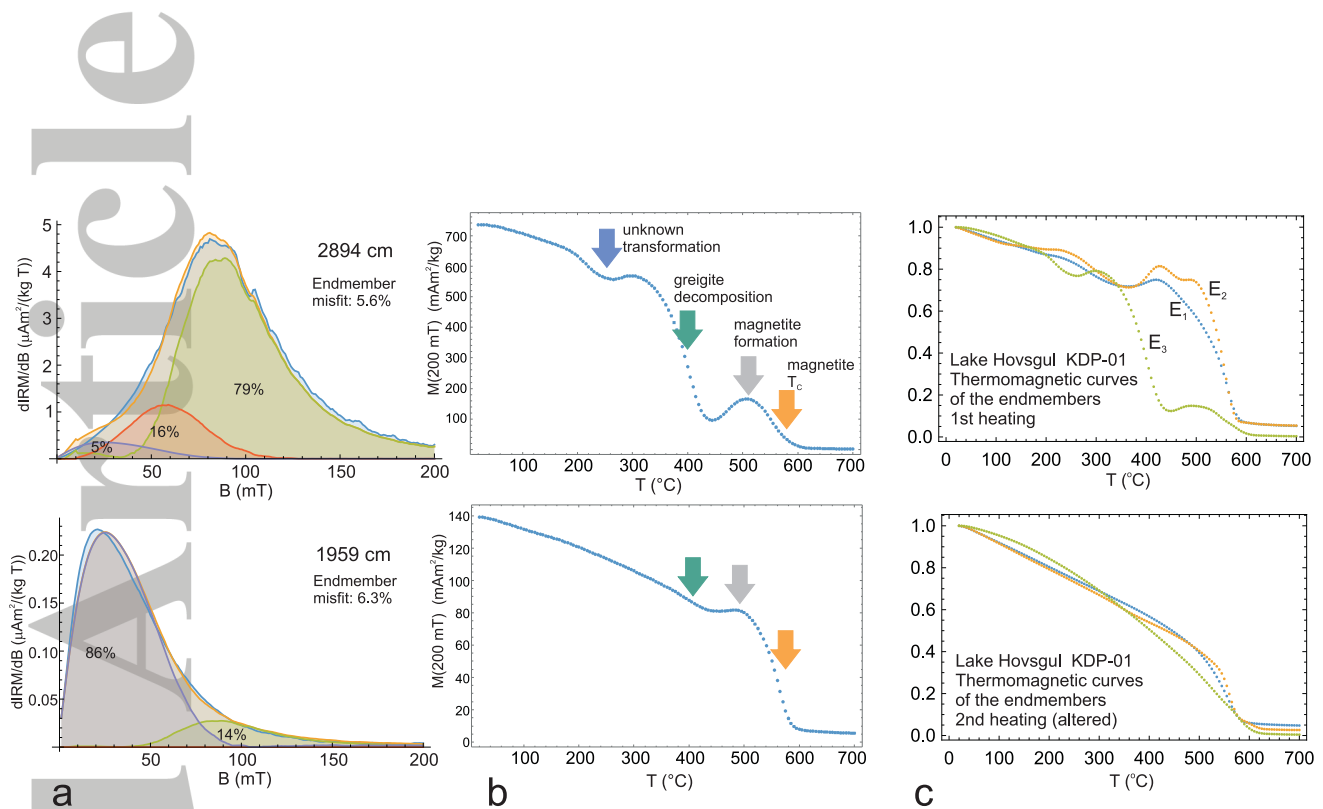


**Figure 5.** a) Two samples with complementary endmember mixtures. Top: At 2894 cm depth the sediment is dominated by 3 (green) Bottom: At 1959 cm the sediment contains mainly endmember 1 (blue) b) Thermomagnetic curves of the first heating for the samples from a). The curve for 2894 cm depth shows a significant drop in magnetization near the typical decomposition temperature whilst at 1959 cm the curve is dominated by a clear drop near the Curie temperature of magnetite. c) Inferred curves of the endmembers from linear decomposition of all 12 available thermomagnetic curves obtained in the field 200 mT. Every curve is normalized to RT-IRM which is room temperature IRM obtained in this field. Top: the decomposition of the first heating curve. Bottom: decomposition of the second heating after alteration.

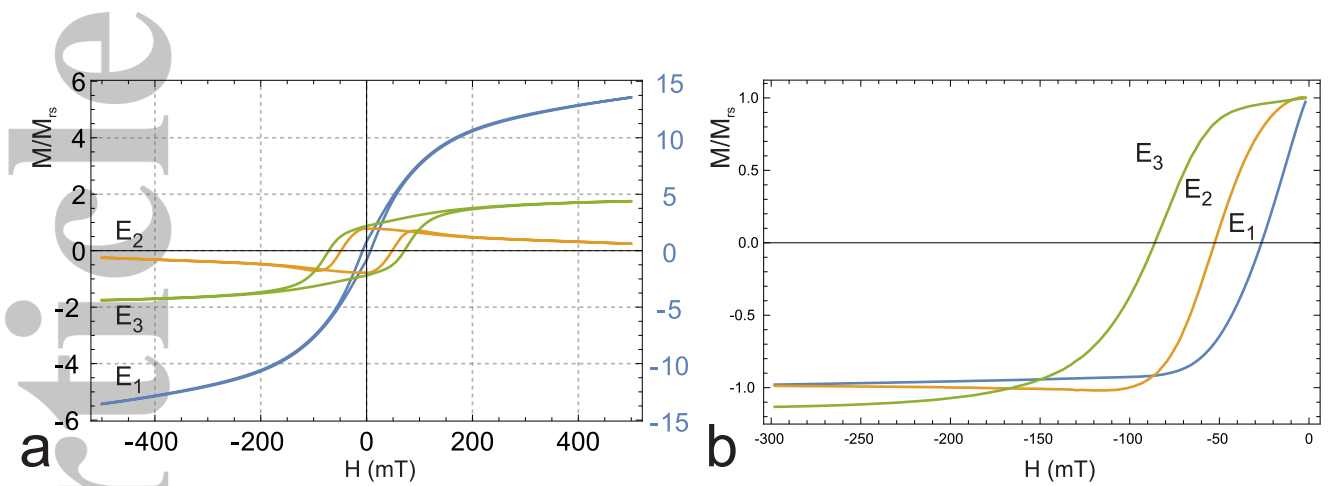


**Figure 6.** a) Reconstructed hysteresis loops corresponding to the three endmembers of the IRM spectra. Right scale:  $E_1$ , left scale:  $E_2, E_3$ . b) Reconstructed backfield curves of the endmembers. The amplitude corresponds to the relative magnetization of the backfield curves with respect to the saturation IRM used for the endmember modeling. The corresponding remanent coercivities  $H_{cr}$  of the three endmembers are: 26 mT, 53 mT and 86 mT.

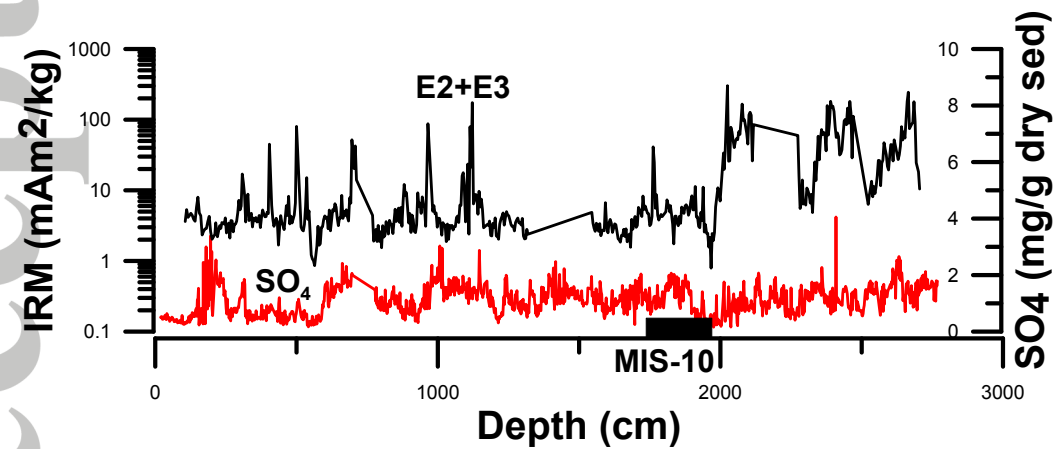


**Figure 7.** Sulfate  $SO_4$  concentration (red line, right axis) and sum of magnetic intensities  $E_2 + E_3$  (black line, left axis) as functions of depth. Black rectangle marks the linearly interpolated position of MIS-10 based on the KDP-01 age model of *Fedotov et al.* [2008].

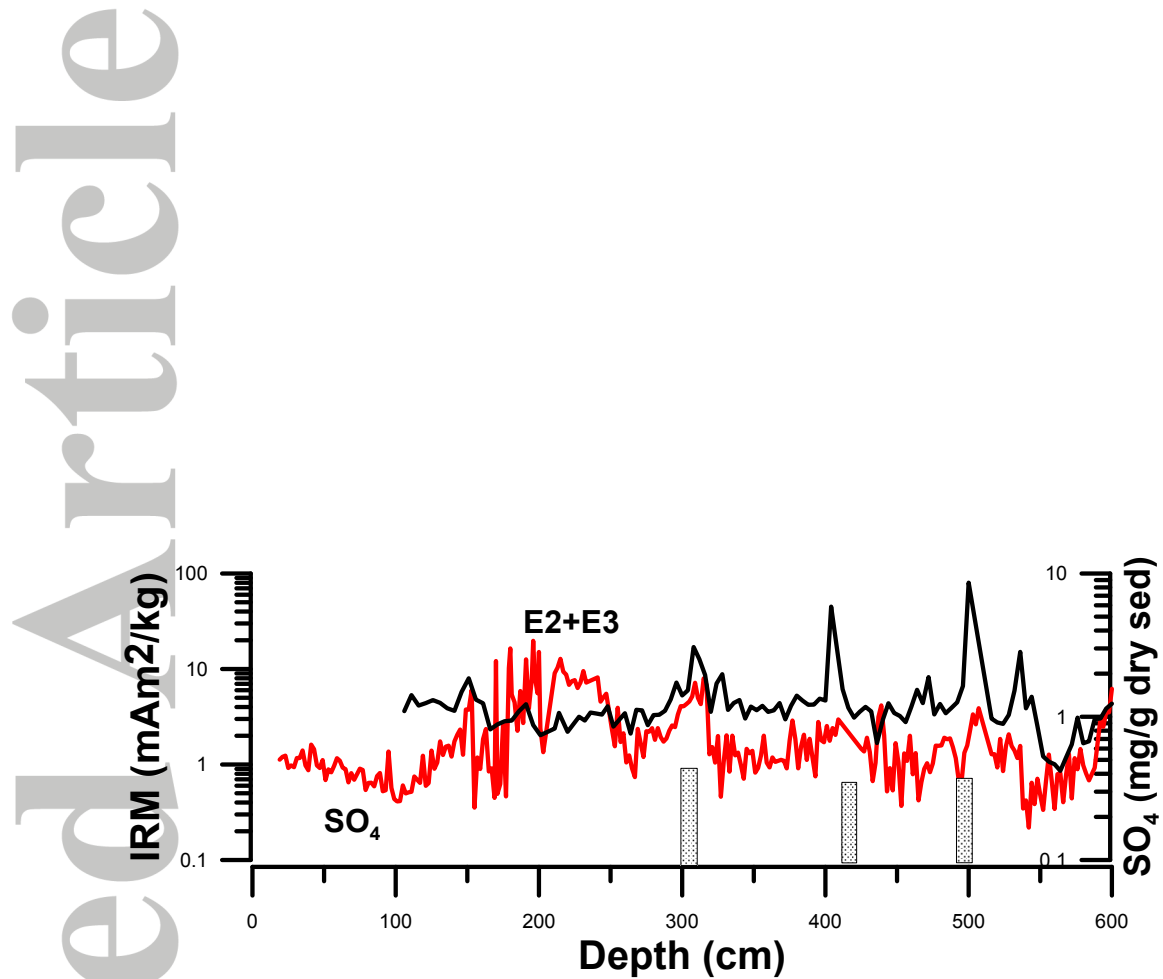


**Figure 8.** Sulfate  $SO_4$  concentration (red line, right axis) and sum of magnetic intensities  $E_2 + E_3$  (black line, left axis) for depths  $< 600$  cm. Bars indicate estimated termination of cold stages MIS-4, MIS-5b and MIS-5d based on the KDP-01 age model of *Fedotov et al.* [2008].

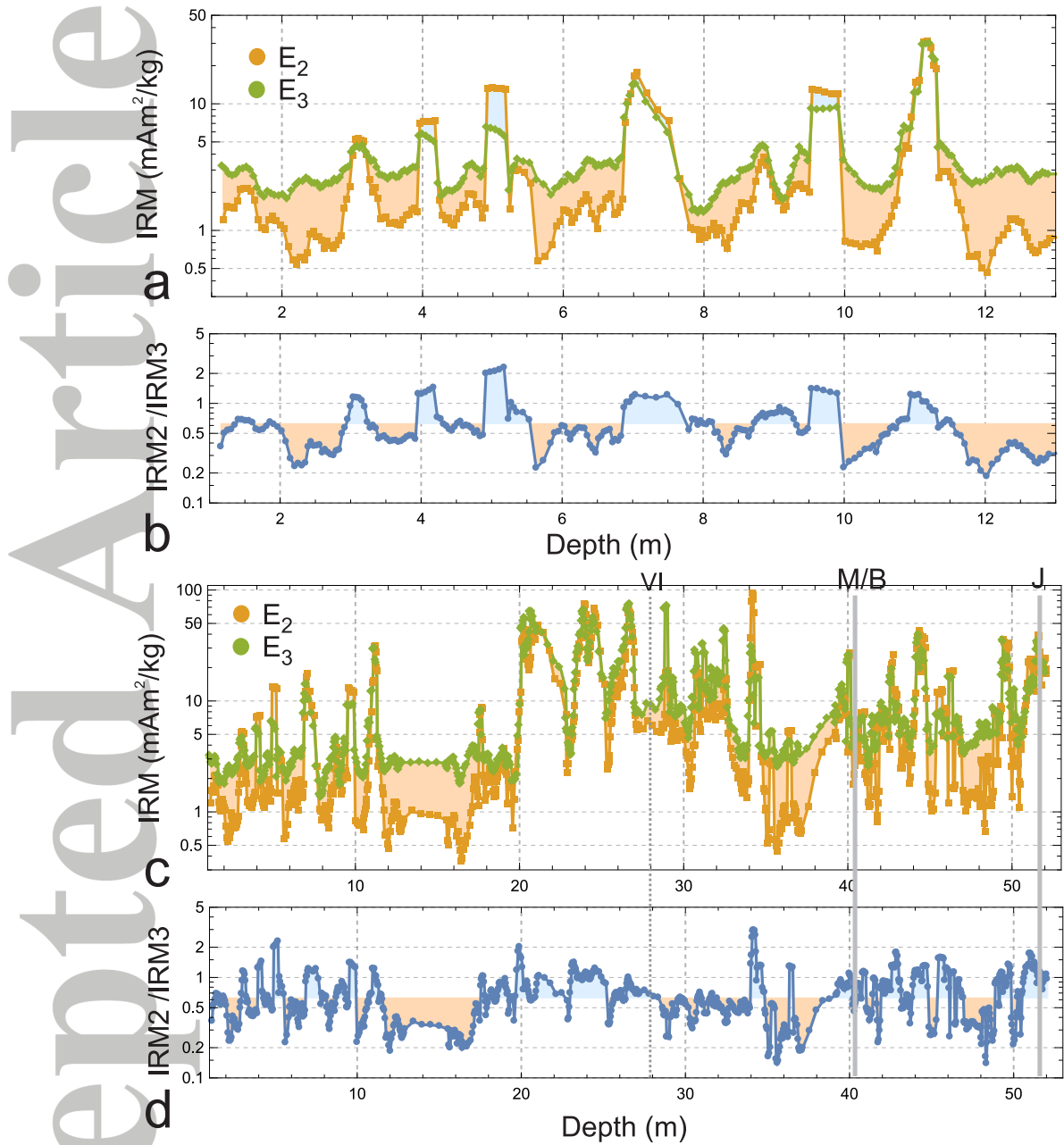


**Figure 9.** a) Five-point smoothed IRM contribution of endmembers  $E_2$  and  $E_3$  for the core top from 1-13 m. Blue filling highlights regions where  $IRM(E_2) > IRM(E_3)$ , orange filling highlights  $IRM(E_3) > IRM(E_2)$ . b) Ratio  $E_2/E_3$  for the core top from 1-13 m. Blue/orange filling highlights regions where  $IRM(E_2)/IRM(E_3)$  is larger/smaller than the median ratio 0.63. c) Like a) but for the whole core from 1-53 m. Dotted line (VI) marks approximate position of a seismic unconformity. Gray lines mark the Matuyama-Brunhes (M/B) transition at about 780 ka and the onset of the Jaramillo subchron at 1 Ma. d) Like b) but for the whole core from

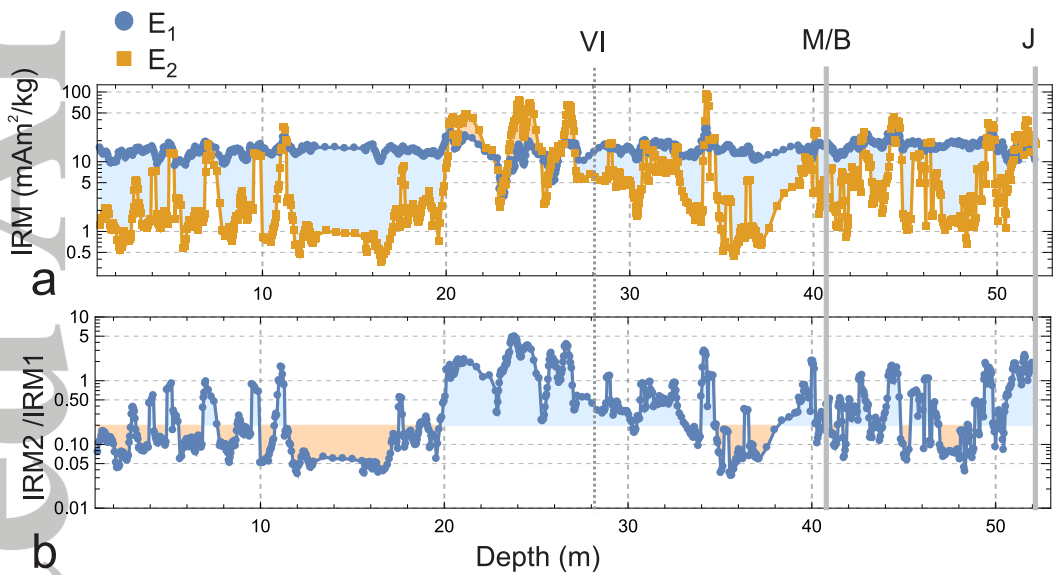


**Figure 10.** a) Five-point smoothed IRM contribution of endmembers  $E_1$  and  $E_2$ . Blue filling highlights regions where  $\text{IRM}(E_2) > \text{IRM}(E_1)$ , orange filling highlights  $\text{IRM}(E_1) > \text{IRM}(E_2)$ . b) Ratio  $E_2/E_1$  for the core from 1-53 m. Blue/orange filling highlights regions where  $\text{IRM}(E_2)/\text{IRM}(E_1)$  is larger/smaller than the median ratio 0.21.